

PRECISION QCD AND ELECTROWEAK PHYSICS AT THE TEVATRON

Norman A. Graf

Brookhaven National Laboratory

Upton, NY 11973

Representing the DØ and CDF Collaborations

ABSTRACT

A brief overview of physics analyses being conducted at Fermilab's Tevatron collider is presented. Selected topics from electroweak and QCD jet analyses undertaken by the DØ and CDF Collaborations are discussed, with an emphasis on those analyses which probe the possible substructure of the Standard Model. In particular, recent results in the inclusive jet production cross section and dijet angular distributions are compared to next-to-leading-order quantum chromodynamics predictions. In the electroweak sector, W and Z boson production properties, trilinear gauge boson couplings, and the W mass are measured and compared to Standard Model expectations.

1 Introduction

The DØ and CDF experiments use large multipurpose detectors to exploit the rich menu of physics produced by the high-energy proton-antiproton ($\bar{p}p$) collisions at Fermilab's Tevatron. The analyses presented here were selected from the large number of topics currently being studied in the data samples accumulated during the period of 1992–1996 and representing in excess of 100 pb^{-1} per experiment. The very large data sets arising from such large integrated luminosities provide very high statistics samples of high transverse energy jets and W and Z bosons, allowing precision tests of the Standard Model (SM) to be carried out. For information on other physics analyses being conducted at the Tevatron, see the talks by DeJongh (“Results from the Tevatron on Heavy Flavor”) and Paterno (“Searches for New Phenomena at the Tevatron”).

Clearly in a talk of this length, not all topics can be discussed, nor can analyses be presented in any great detail. It is intended to be a general description for an audience composed of both students and physicists not necessarily expert in these fields.

For completeness, a brief overview of the accelerator is provided, followed by a discussion of the two collider detectors at the Tevatron, DØ and CDF. A rudimentary description of particle and jet identification is then presented.

The QCD and electroweak analyses which are presented were selected to reflect not only the most recent advances, but also those topics which one can probe beyond the SM. Despite its remarkable success, it is felt by many that the SM will eventually be replaced by a more fundamental theory of the elementary particles and their interactions. Confronting the SM predictions with precision experimental tests is expected to eventually reveal shortcomings and pave the way to a better, more complete understanding of the underlying forces of nature. The topics were chosen, therefore, to illustrate those analyses which probe the substructure of the SM.

Just as the unexpectedly hard scattering of α particles off gold foil provided evidence for the nucleus, so too, could anomalous scattering in $\bar{p}p$ interactions provide evidence for possible quark substructure. This is what motivates the two QCD jet analyses. The first investigates the inclusive jet cross section, searching for any signs of excess jet production at high transverse energies (E_T). The highest E_T jets probe distance scales on the order of 10^{-17} cm, almost an order

of magnitude smaller than the weak scale, and have a cross section much smaller than even top quark production. The second analysis also searches for quark compositeness, this time by analyzing the angular distribution of dijet final states. Standard Model QCD dijet production results in angular distributions which are peaked at small center-of-mass scattering angles; the decay of heavy objects would lead to a more isotropic angular distribution. Comparing the measurements with predictions allows limits to be set on the mass scale for any quark compositeness.

The electroweak sector of the SM has experienced many spectacular successes, from the predictions of the vector boson masses to the recently discovered top quark mass. The bulk of this talk concerns itself with rigorous tests of the SM predictions for various electroweak processes. Numerous properties of the vector bosons are investigated, from cross-section measurements to checks for anomalous production, to a measurement of the width of the W boson, to searches for non-SM decay modes into supersymmetric particles or heavy quarks. The high energy of the Tevatron allows an investigation of the Drell-Yan process at very high dilepton invariant masses, where the effects of possible quark substructure would manifest themselves. The gauge structure of the electroweak sector places very strict constraints on the gauge boson self-couplings. In keeping with the main thrust of this talk, only the $W-\gamma$ channel is discussed, where the couplings can be related to the W boson electric and magnetic multipoles. Anomalous couplings would, therefore, directly indicate substructure similar to the neutron's anomalous magnetic moment. Finally, the focus is turned to the W boson mass measurement. The Born level predictions for the mass are modified by higher-order corrections which depend on both the top quark mass and the as yet undiscovered Higgs mass. A precise measurement of the W boson mass, combined with the recently measured top quark mass, can thus be used to place constraints on the Higgs mass. Alternatively, evidence for non-SM behavior may be discovered.

2 The Tevatron

Fermi National Accelerator Laboratory is located near Chicago in the USA and is home to the world's highest energy particle accelerator, the one-kilometer radius Tevatron. The Tevatron provides experimentalists with $\bar{p}p$ collisions at a center of mass energy of 1.8 TeV with delivered luminosities of $\sim 10^{31} \text{cm}^{-2}\text{s}^{-1}$. The DØ and CDF detectors are housed in two of the interaction regions, with a Gaussian

luminous region with $\sigma \sim 30$ cm along the beam and beam profiles $\sim 40 \mu\text{m}$ in the transverse dimension. The time between crossings of the bunches is $3.5 \mu\text{sec}$. Figure 1 is a sketch showing the locations of the accelerators and detectors. Both experiments collected roughly 100 pb^{-1} of data during Run 1; $\sim 20 \text{ pb}^{-1}$ in 1992–1993 (Run 1a) with the remainder $\sim 90 \text{ pb}^{-1}$ in 1994–1995 (Run 1b).

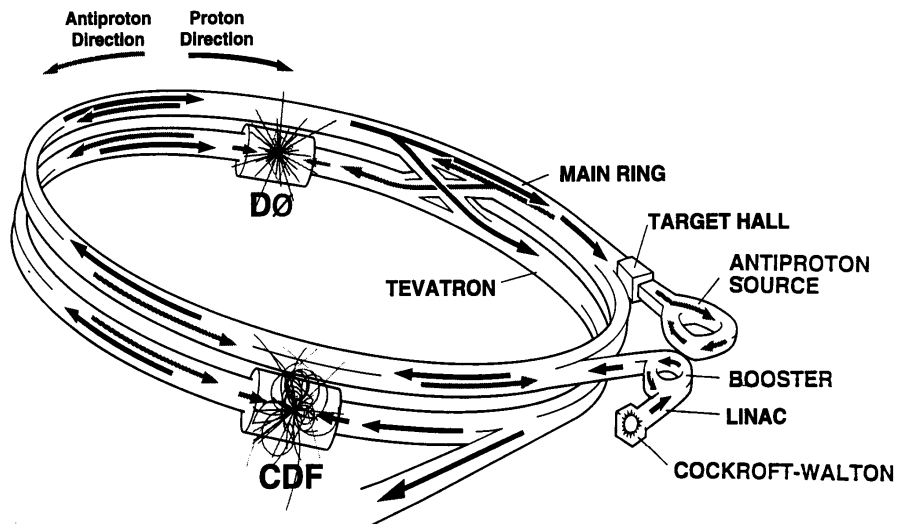


Fig. 1. The Fermilab accelerators and collider detectors.

3 The Collider Detectors

The $D\bar{O}$ and CDF^1 experiments utilize large multipurpose detectors (Fig. 2 and Fig. 3) composed of many subsystems to detect the myriad final-state products arising from $\bar{p}p$ annihilations. Both detectors employ drift chambers to track charged particles from the interaction region to the calorimeter. The CDF detector has enjoyed the advantage of an upgraded silicon vertex detector which provides very high resolution tracking near the vertex. A central solenoidal magnetic field allows the momenta of charged particles to be measured. $D\bar{O}$ has a very compact, nonmagnetic central tracking volume. Both detectors have massive segmented sampling calorimeters to contain and measure the energies of electromagnetic and hadronic showers. The compact and hermetic $D\bar{O}$ calorimetry utilizes uranium and liquid-argon housed in three cryostats, whereas CDF employs scintillator-based calorimetry. Outside the calorimeters of both experiments are

CDF Detector

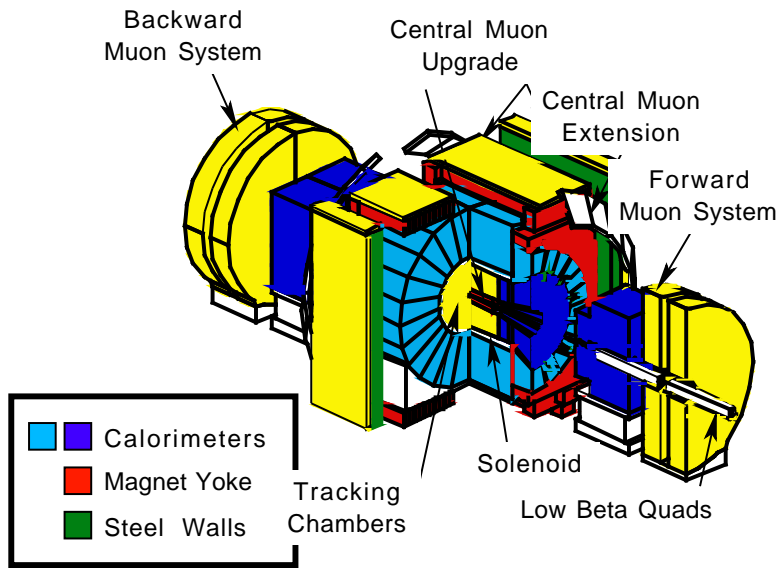
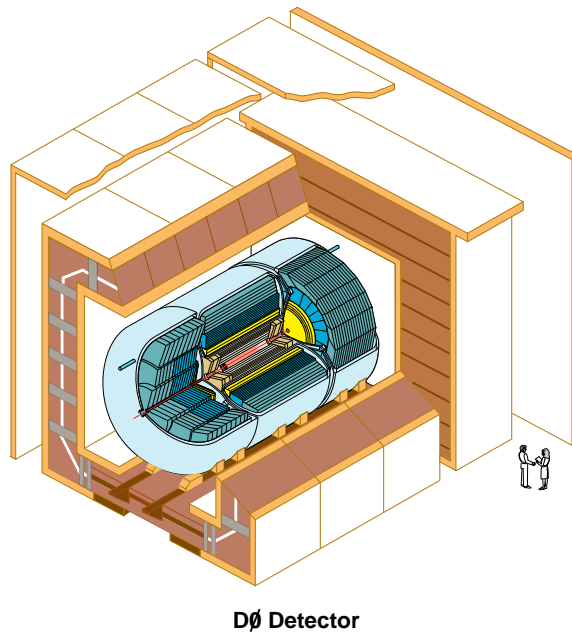


Fig. 2. The CDF Detector.



DØ Detector

Fig. 3. The DØ Detector.

additional drift chambers used to detect the passage of muons which escape the calorimeter. The $D\bar{O}$ muon system uses toroidal magnetic fields to measure the muon momentum. The analyses which follow are based on event reconstructions employing jets, electrons, muons, and neutrinos. (Tau leptons are reconstructed in the collider environment only with great difficulty due to the large hadronic backgrounds.) Brief descriptions of the particle identification algorithms are presented here for completeness.

Jets are reconstructed in both detectors by clustering energy depositions in the calorimeters using a fixed cone algorithm. Corrections are then applied to account for energy losses outside the cone as well as for nonlinearities in the detectors' low energy response, and inclusion into the cone of energy deposits from the underlying event and multiple interactions in the same beam crossing.

Both experiments identify electrons by detecting their isolated electromagnetic showers in the calorimeters. The longitudinal and lateral developments of these showers are required to be consistent with expectations from test beam measurements and Monte Carlo simulations. Additionally, tracks in the central tracking volume are required to point to the shower. CDF further insists that the momentum of the track match the energy of the electromagnetic (EM) cluster, whereas $D\bar{O}$ uses the ionization along the track and information gathered from a Transition Radiation Detector (TRD) in the central region to provide additional confirmation.

Muons, interacting only minimally in the calorimeters, are detected in the outer muon chambers. In CDF, the muon momentum is derived from the matching inner central track, whereas in $D\bar{O}$ the momentum is measured in the toroidal field of the outer muon magnetic system.

The presence of neutrinos is inferred from an imbalance in the transverse energy distribution derived by vectorially summing the calorimeter energy depositions and accounting for muons. Since initially the $\bar{p}p$ system has only minimal transverse momentum, any final imbalance must be due to mismeasurement arising from detector resolution or inhomogeneities, or to undetected particles. However, only information about the transverse energy of the neutrino can be inferred by this method; no information about the longitudinal momentum is available.

4 QCD Physics

4.1 Introduction

Quantum Chromodynamics (QCD) is the current theoretical framework for describing the physics of strong interactions. One of the most fundamental of QCD processes to be studied at the Tevatron is that of jet production. Dijet final states are copiously produced in $\bar{p}p$ collisions at $\sqrt{s} = 1800$ GeV through quark-antiquark annihilation and quark-quark, quark-gluon, or gluon-gluon scattering. Leading order (LO) QCD has been very successful in explaining theoretically the dynamics of such two-to-two processes. At high momentum transfer scales (Q^2), the theory can be calculated perturbatively, leading to finite predictions for the dijet cross section. However, experiments do not detect bare partons. They detect and reconstruct jets of associated particles and these jets are identified with partons. Furthermore, parton evolution, hadronization, and vagaries of detector response and efficiencies conspire to smear out this one-to-one association.

The study of QCD processes at a hadron collider is further complicated by the fact that one is not colliding partons; at the Tevatron, beams of protons and antiprotons are caused to collide. The hard scattering occurs between partons sampled from the hadrons; the lack of knowledge about the exact structure of the hadrons is partially masked by the introduction of structure functions, or parton distribution functions (pdf's). These are phenomenological distributions fit to experimental data and assumed to be universally valid. Figure 4 presents a cartoon of a LO QCD interaction at the Tevatron. Quarks with momentum fractions x_1 and x_2 are sampled from the antiproton and proton, respectively. These quantities are, of course, unknowable on an event-by-event basis; one integrates over the pdf spectrum when performing calculations. (It should be pointed out that pdf's have not yet been accurately determined at the highest energies accessible by the Tevatron.) The choice of pdf introduces variances on the order of 10% in the final cross section. The exchange of a gluon leads to the diquark parton final state, which then hadronizes and is detected in the experimental apparatus.

The spectrum of final states which is produced in nature is, however, much richer in detail and intricacy than that predicted by LO QCD. Initial and final state radiation conspire to produce additional partons with much lower energies, thus introducing additional Q^2 scales to the calculations which, along with

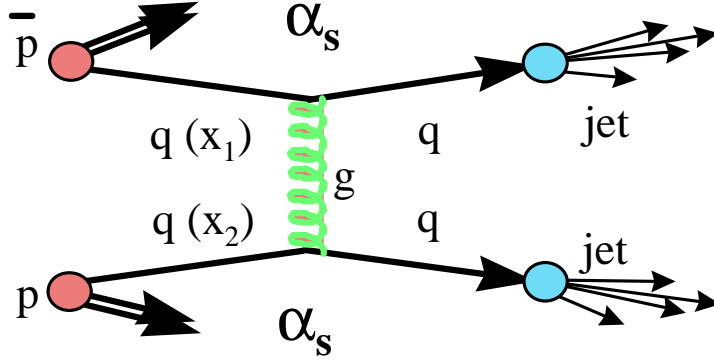


Fig. 4. Leading order QCD diagram of $q\bar{q}$ scattering at the Tevatron. Quarks, sampled from the hadrons with momentum fractions x_1 and x_2 , undergo a hard scatter via exchange of a gluon, and then hadronize, to be detected in the experimental apparatus as jets of particles.

collinear divergences, make the predictions much more difficult to calculate. Next-to-leading-order (NLO) QCD attempts to improve the theoretical understanding of multijet production by allowing for a third parton and calculating the two-to-three matrix elements. In order to compare the theoretical predictions with experimental measurements, one must introduce a jet algorithm which clusters partons into jets. A parameter R_{sep} is introduced which specifies the separation in $\eta - \phi$ space below which two partons will be coalesced into a single jet. DØ requires the final state partons to be within one cone width (R) of their summed E_T vector direction and within $R_{sep} = 1.3$ of one another; CDF uses $R_{sep} = 2.0$. The NLO process illustrated in Fig. 5 can result in either a two- or three-jet final state, depending not only on the phase space distribution of the additional radiation with respect to the outgoing parton, but also on the NLO jet algorithm and the specifics of the evolution and hadronization of the partons. Indeed, a NLO three-jet final state could be detected by the experiment as a two-jet system due to these effects, and vice versa.

There is also a continuum of behavior between higher order QCD corrections and hadronization which NLO QCD only begins to address. The truncation of the calculation at order α_s^3 therefore results in a residual dependence on the renor-

malization scale at which the calculation is performed, introducing an uncertainty on the order of 10–15%. DØ chooses this renormalization scale to be equal to half the maximum jet transverse energy in the event ($E_{T(max)}/2$), whereas CDF opts for $E_{T(Jet)}/2$. The experimental picture is also clouded by this extra complexity, since low-energy partons do not efficiently express themselves as jets in the experimental detectors, due either to their proximity to the primary jets or to their much lower energy.

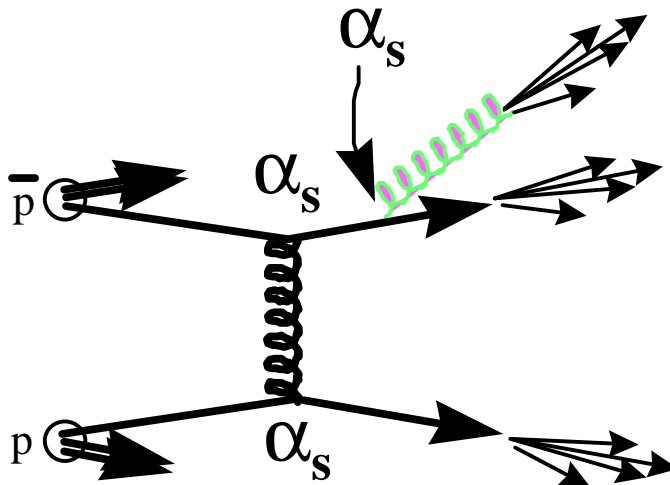


Fig. 5. Next-to-leading order QCD diagram illustrating the additional complexity introduced by higher order terms.

4.2 Inclusive Jet Cross Section

Measuring the cross section for inclusive jet production ($\bar{p}p \rightarrow \text{jet} + X$) is one of the most fundamental measurements which one can make at the Tevatron, since jets are copiously produced in hadron collisions. Furthermore, recent NLO QCD calculations provide relatively precise predictions of the inclusive jet cross sections. Ellis, Kunszt, and Soper² have published analytic predictions and Giele, Glover, and Kosower³ have provided a Monte Carlo program (JETRAD) which generates events with final state partons. This feature allows one to study the effects of jet resolution, efficiencies, and detector acceptances. These recent

advances allow precise comparisons to be made between theoretical predictions and the experimentally measured distributions.

Figure 6 shows the cross section for inclusive jets detected in the central rapid-

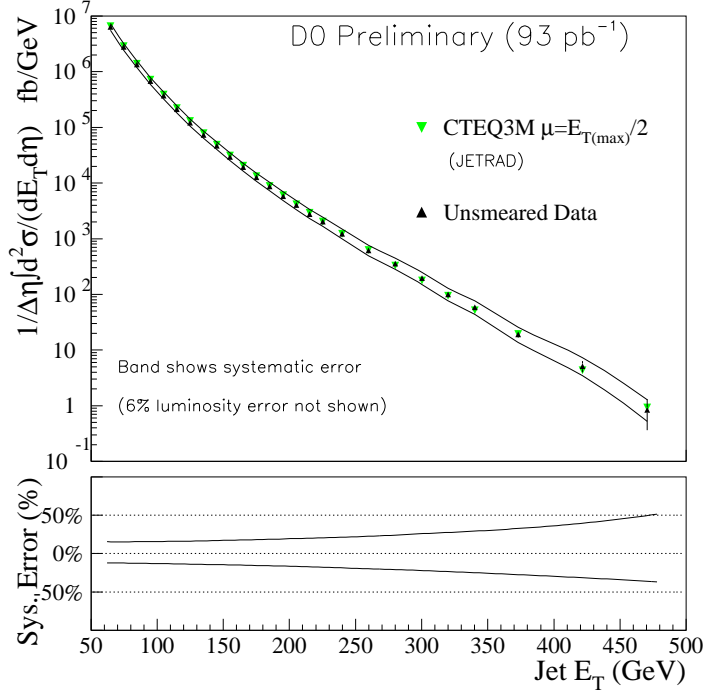


Fig. 6. The central inclusive jet cross section as a function of jet transverse energy as measured by DØ, showing excellent agreement between data and theory over seven orders of magnitude.

ity interval ($|\eta| < 0.5$) of the DØ detector as a function of jet E_T . The error bars on the data points include statistical as well as uncorrelated systematic uncertainties. The theoretical predictions, using the CTEQ3M pdf's and a renormalization scale μ equal to the maximum jet $E_T/2$ are superimposed on the plot. The theoretical uncertainties are depicted by the solid lines above and below the data points. The systematic uncertainty, comprised almost entirely of the jet energy scale uncertainty, is depicted in the lower plot. The agreement, over seven orders of magnitude, is seen to be excellent.

The CDF Collaboration has previously published the results of their inclusive jet analysis⁴ from the Run 1a data sample. This analysis indicated an excess in jet production at large jet E_T over expectations, as shown in Fig. 7. The inclusive

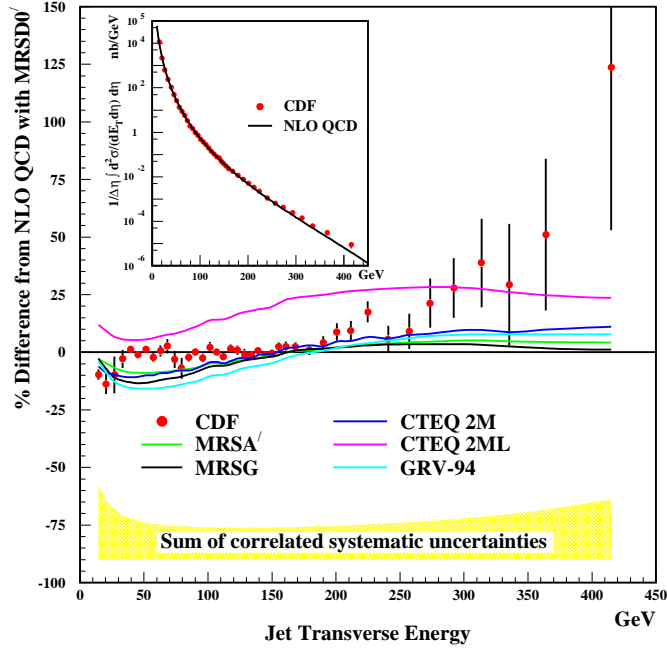


Fig. 7. The central inclusive jet cross section as measured by CDF (inset), and the deviation from NLO theoretical predictions $[(\text{Data}-\text{Theory})/\text{Theory}]$ as a function of jet transverse energy.

central ($0.1 \leq |\eta| \leq 0.7$) jet cross section as a function of jet E_T is shown in the inset. To highlight the comparison to the theoretical expectations, which can be lost in a semi-logarithmic plot, the distribution of $[(\text{Data}-\text{Theory})/\text{Theory}]$ is presented. The theory is that of Ellis, Kunszt, and Soper² with the *MRSD0'* pdf's. There is relatively good agreement below 200 GeV, but an appearance of an excess at higher E_T . A preliminary analysis of the full data set exhibits similar behavior. The presence of quark substructure would be expected to manifest itself as just such an enhancement. However, due to uncertainties in both the theoretical calculations and the parton distribution functions at such high Q^2 values, no claim for evidence of new physics beyond the SM can be made. The corresponding plot for the $D\bar{O}$ inclusive jet data is presented in Fig. 8, where the data and theory are seen to be in very good agreement over the full range of energies. In order to check these results, the $D\bar{O}$ Collaboration has repeated its analysis, using the CDF fiducial cuts, and compared the preliminary CDF Run 1b results with a fit to the $D\bar{O}$ data. The results are shown in Fig. 9. Within the systematic

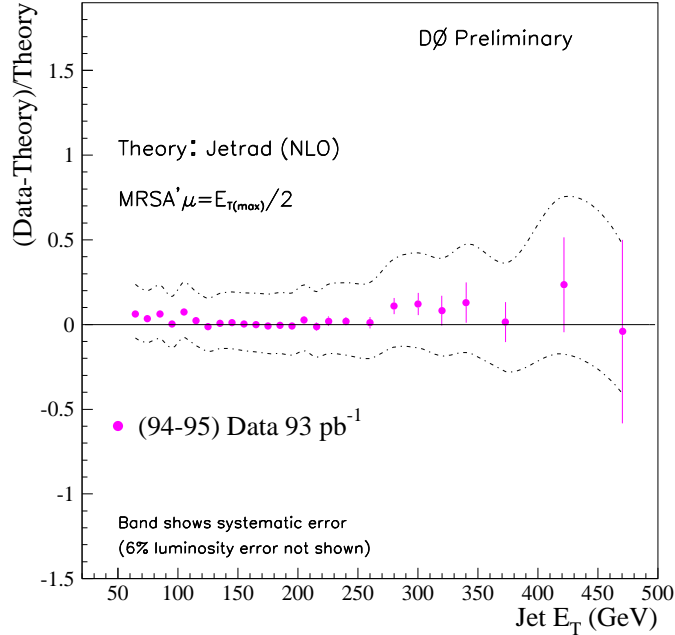


Fig. 8. $[(\text{Data}-\text{Theory})/\text{Theory}]$ as a function of jet transverse energy for the DØ inclusive jet data as a function of jet E_T , showing good agreement with NLO QCD over the full energy range.

uncertainties, the results of the two experiments agree. The experiments differ, however, in their interpretations of the agreement (or lack thereof) of the data with the theoretical predictions. The large systematic uncertainties in both the experimental measurements and the theoretical calculations allow for the interesting situation wherein the CDF and DØ measurements are commensurate with one another, yet CDF claims a disagreement with theory and DØ claims excellent agreement.

4.3 Dijet Angular Distributions

At a hadron collider, QCD parton-parton scattering processes proceed predominantly through t-channel exchanges, resulting in dijet angular distributions which are peaked at small center-of-mass scattering angles. Moreover, final states arising from quark-quark, quark-gluon, and gluon-gluon interactions are predicted by theory to produce similar angular distributions. Therefore, when analyzing dijet

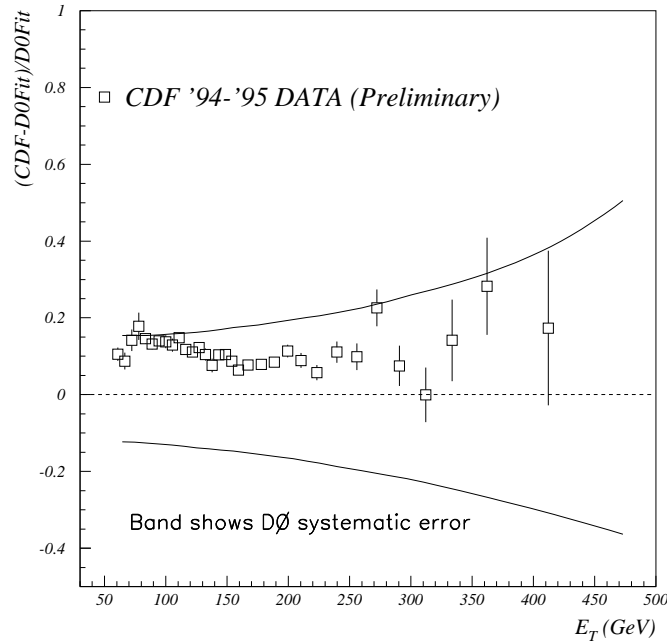


Fig. 9. A comparison of the CDF and DØ data. The DØ data have been reanalyzed using the CDF fiducial cuts. The CDF data points have then been compared to a fit to the DØ spectrum. The band shows the DØ systematic uncertainty.

angular distributions the effects of uncertainties in the parton distribution functions for the interacting partons are suppressed, leading to a greater sensitivity to physics beyond the SM. For instance, dijet final states resulting from interactions between quark constituents are expected to be produced isotropically, and would therefore lead to a perturbation of the angular distributions of jets. Quantifying the agreement between the experimentally observed spectrum and that predicted by perturbative QCD allows limits to be placed on the mass scale for such new interactions.

If one hypothesizes that quarks are bound states of preons which interact via a new strong interaction, one can characterize the strength of this interaction with a mass scale Λ . For $\sqrt{\hat{s}} \ll \Lambda$ the substructure interaction can be represented by contact terms. The dijet cross section then becomes

$$d\sigma \sim \alpha_S(\mu^2) + \alpha_S(\mu^2) \frac{\hat{s}}{\Lambda^2} + \left(\frac{\hat{s}}{\Lambda^2}\right)^2,$$

viz. terms proportional to the QCD, interference, and compositeness interactions, respectively. The last two terms result in a dijet angular distribution

proportional to $(1 + \cos\theta^*)^2$. To flatten out the $\cos\theta^*$ distribution and to facilitate comparison to the theoretical predictions, one introduces a new variable $\chi = (1 + \cos\theta^*)/(1 - \cos\theta^*)$. Rutherford scattering ($\sim 1/(1 - \cos\theta^*)^2$) produces a flat $dN/d\chi$ distribution, whereas heavy objects decaying isotropically enhance the $\chi \sim 1$ region.

Figure 10 presents the $D\bar{O}$ dijet angular distribution in four regions of dijet invariant mass. The data are seen to be in somewhat better agreement with the NLO theoretical predictions than with the LO predictions, especially at large values of χ , although the sensitivity to the renormalization scale is seen to be large. All systematic uncertainties were added in quadrature and are presented as bands at the bottom of the figures.

Based on a comparison of the data with theoretical expectations, one can extract limits on the mass scale for quark compositeness. Previously published results⁵ have presented model-dependent limits of $\Lambda > 1.6$ – 1.8 TeV. Results are presented here from a recent analysis by the $D\bar{O}$ Collaboration⁶ of its full Run 1 data sample. Since no currently available NLO calculations implement quark compositeness, an LO simulation⁷ was used to search for possible effects of quark substructure. The ratio of LO predictions with and without compositeness was used to scale the NLO QCD predictions. Figure 11 shows the dijet angular distributions for events with a dijet invariant mass above 635 GeV along with predictions using various values of the contact term Λ . The highest dijet invariant mass region was chosen since the effects of quark compositeness are expected to become more pronounced in this region. To extract a limit on the compositeness scale, a Bayesian technique using a Gaussian likelihood function for the ratio of events above and below $\chi = 4$ was employed. The compositeness limit therefore depends on the renormalization scale μ , the model for the compositeness, and the choice of prior probability distributions. For models with left-handed contact interference, the 95% confidence level lower limit on the interaction scale Λ is 2.1 TeV for $\mu = E_T^{max}$, rising to 2.3 TeV for $\mu = E_T^{max}/2$.

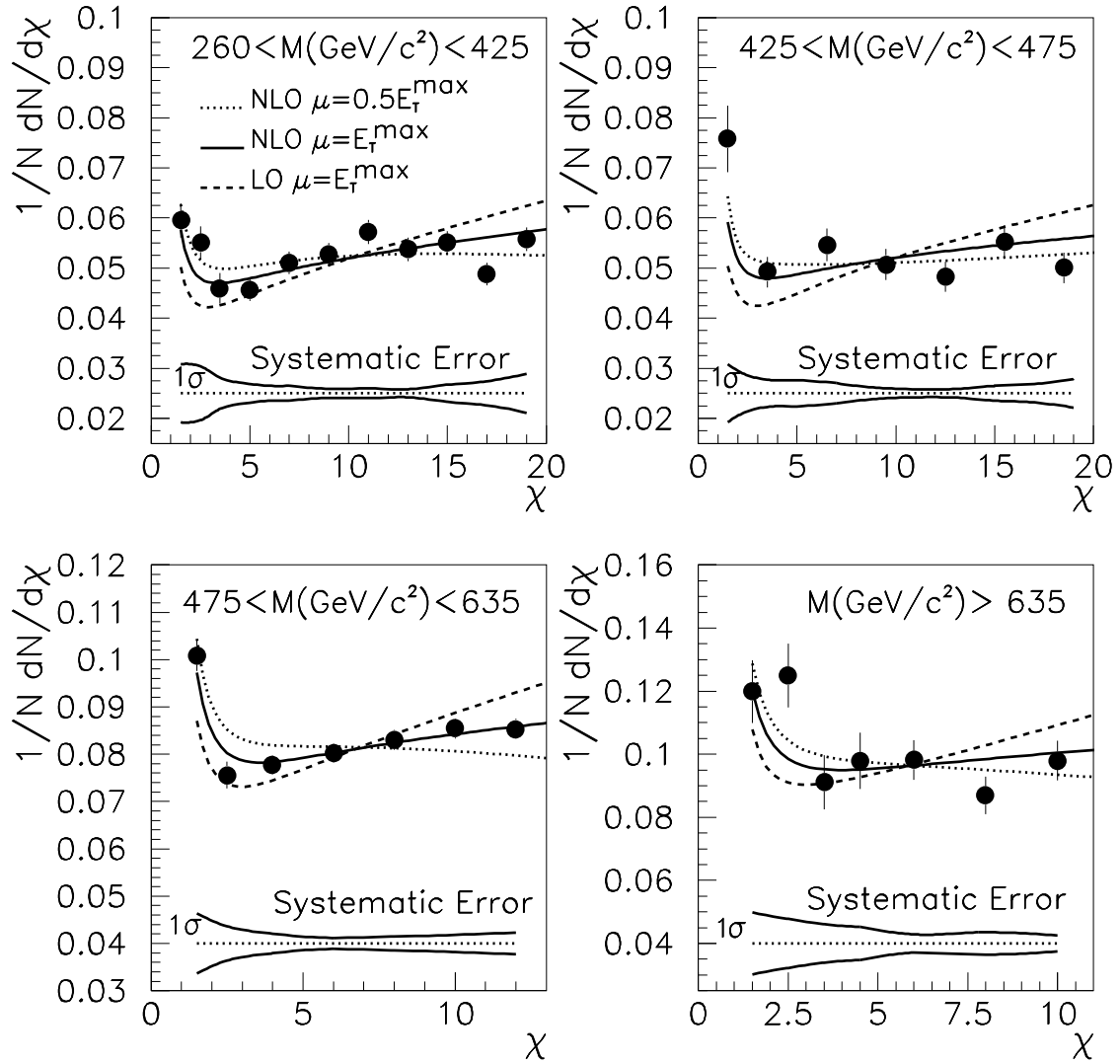


Fig. 10. Dijet angular distributions for $D\bar{O}$ data compared to JETRAD LO and NLO predictions in various dijet mass bins. Uncertainties on the data points are statistical while the band represents the correlated systematic uncertainties.

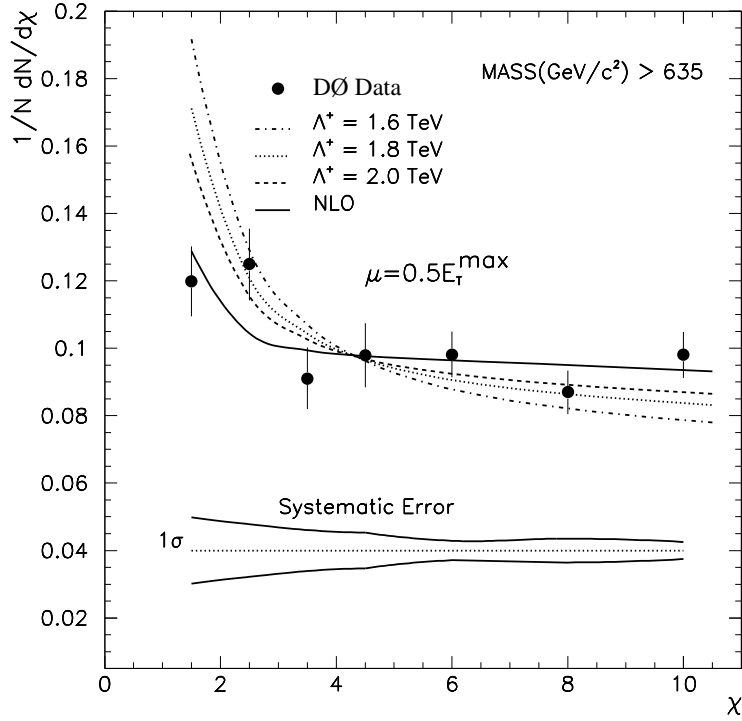


Fig. 11. Dijet angular distribution for $D\bar{O}$ events in the highest mass bin along with NLO predictions for various compositeness scales. Note how heavy objects decaying isotropically enhance the $\chi \sim 1$ region. Uncertainties on the data points are statistical while the band represents the correlated systematic uncertainties.

5 Electroweak Physics

Electroweak physics encompasses the interactions of W and Z bosons.

Although the intermediate vector bosons decay predominantly into pairs of quarks, they are detected in both CDF and $D\bar{O}$ through their leptonic decays. This is due to the overwhelming production of dijet events through ordinary QCD and the impossibility of uniquely identifying dijet final states as arising from W or Z boson decays. The final state leptons are characterized by high momenta and tend to be quite isolated from other activity in the event. Z bosons are detected by identifying pairs of high transverse momentum (E_T) electrons or muons (taus are not uniquely identified, nor are neutrinos individually detectable). The invariant mass of the dilepton system can then be reconstructed, giving rise to a peak at the Z in the dilepton invariant mass distribution, with a background from the

Drell-Yan continuum production of dilepton pairs. The purity of the sample can be directly determined by measuring the number of events which lie outside the peak region (and after accounting for the Drell-Yan continuum). Figure 12(a) shows the dielectron invariant mass spectrum measured at DØ from the Run 1b data sample.

W bosons are detected by their decay into a lepton and its associated neutrino. Since no information is available about the longitudinal momentum of the neutrino, only so-called “transverse” properties of the W boson can be directly measured. The final-state signature of a W boson decay consists of a high E_T electron or muon and a significant amount of missing transverse energy. From this information, the transverse mass (M_T), which is the two-dimensional analogue of the invariant mass, is reconstructed as $M_T = \sqrt{2E_T^e E_T^\nu (1 - \cos\phi^{e\nu})}$. This distribution exhibits a sharp Jacobian peak at roughly the mass of the W boson, with a tail extending down to lower masses. There is, however, no explicit analytic form for this distribution. Figure 12(b) shows the $e\nu$ transverse mass spectrum for W boson candidate events as measured at DØ from the Run 1b data sample.

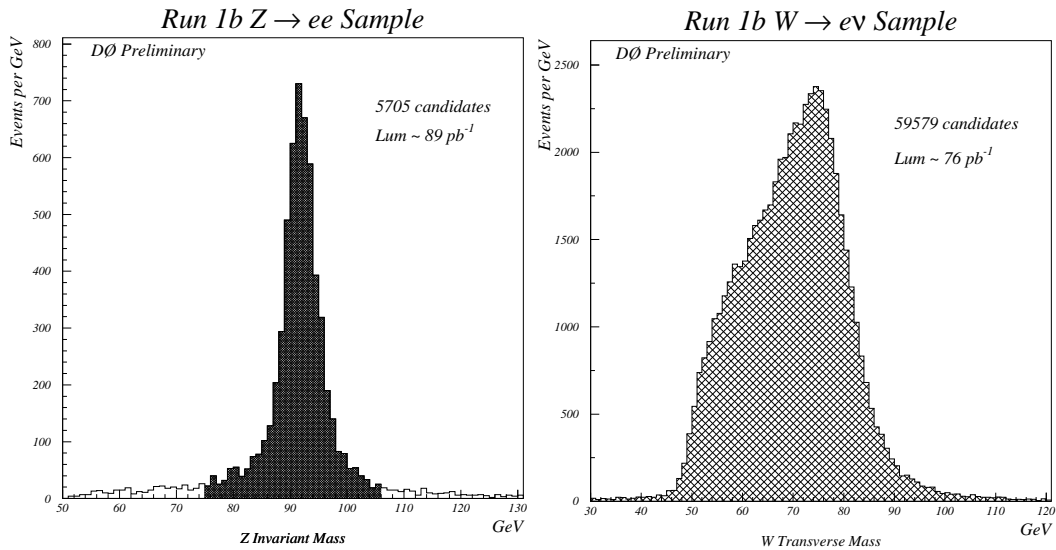


Fig. 12. (a) The dielectron invariant mass distribution and (b) the transverse mass distribution for $W \rightarrow e\nu_e$ candidates at DØ.

5.1 Vector Boson Production Properties

5.1.1 W and Z Production Cross Sections

The cross sections for W and Z boson production at the Tevatron are measured indirectly through the cross section times branching ratio into leptons. This measurement provides not only a comparison to theoretical predictions, but also provides a method to indirectly measure the total width of the W boson, thereby providing information on all of its decay channels. As can be seen from Table 1,

	$\sigma_W \cdot B(W \rightarrow \ell\nu)nb$	$\sigma_Z \cdot B(Z \rightarrow \ell\ell)nb$
DØ (e)	$2.38 \pm 0.01 \pm 0.22$	$0.235 \pm 0.003 \pm 0.021$
DØ (μ)	$2.28 \pm 0.04 \pm 0.25$	$0.202 \pm 0.016 \pm 0.026$
CDF (e)	$2.49 \pm 0.02 \pm 0.12$	$0.231 \pm 0.006 \pm 0.011$
CDF (μ)	$2.48 \pm 0.03 \pm 0.16$	$0.203 \pm 0.010 \pm 0.012$
Standard Model	$2.42^{+0.13}_{-0.11}$	$0.226^{+0.011}_{-0.009}$

Table 1. W and Z production cross sections times leptonic branching ratio. The first uncertainties are statistical only, the second include systematic uncertainties arising from the detector efficiencies and acceptances as well as the luminosity measurement.

the direct measurements of the W and Z boson production cross sections^{8,9} are dominated by the systematic uncertainties of the detector acceptances and efficiencies as well as the integrated luminosity. The theoretical predictions are also limited by the precision with which the pdf's are known. However, by taking the ratio of W to Z boson cross sections, many of these systematic uncertainties disappear or are to a large extent cancelled. Additionally, information about the inclusive width of the W boson can be derived from this ratio. Comparing the experimentally measured value of the width to that predicted by the Standard Model can shed light on any nonstandard decays of the W boson, since any additional decay modes will lead to an increase in the W width. Theoretically, the ratio R can be expressed as a combination of factors which are either well measured or

precisely calculable as follows:

$$\mathbf{R}_\ell = \frac{\sigma \cdot \mathbf{B}(\mathbf{W} \rightarrow \ell\nu)}{\sigma \cdot \mathbf{B}(\mathbf{Z} \rightarrow \ell\ell)} = \frac{\sigma_{\mathbf{W}}}{\sigma_{\mathbf{Z}}} \cdot \frac{\Gamma(\mathbf{Z})}{\Gamma(\mathbf{Z} \rightarrow \ell\ell)} \cdot \frac{\Gamma(\mathbf{W} \rightarrow \ell\nu)}{\Gamma(\mathbf{W})}.$$

Combining the published ratios of W and Z cross sections for the two experiments results in a value of $\mathbf{R}_\ell = 10.90 \pm 0.32$, from which one derives a value for the W width of $\Gamma_W = 2.043 \pm 0.062$ GeV. Comparing this to the SM prediction of $\Gamma_W = 2.077 \pm 0.014$ GeV allows one to set a 95% confidence level upper limit of $\Gamma < 109$ MeV on non-SM decays of the W.

A direct measurement of the W width has been conducted at CDF by measuring the high end of the transverse mass distribution and comparing it to that derived from a Monte Carlo simulation.¹⁰ The value of $\Gamma_W = 2.11 \pm 0.32$ GeV is less precise, but in good agreement with the value extracted from the ratio of cross sections.

5.1.2 W Asymmetry

Uncertainties in the parton distribution functions contribute rather substantially to the uncertainties in many of the electroweak measurements undertaken at the Tevatron. Constraints on these distributions can be extracted from the lepton charge asymmetry arising from W boson decays. In $\bar{p}p$ annihilations, $W^+(W^-)$ bosons are produced mainly from $u\bar{d}(d\bar{u})$ quark pairs. Due to the stiffer momentum distribution of u quarks in the proton compared to d quarks, $W^+(W^-)$ bosons tend to be boosted along the proton (antiproton) direction. The decay products of the W boson are then distributed according to the well-known V-A coupling and tend to be boosted in the same direction as the boson itself. Therefore, by measuring the asymmetry in the charged lepton distributions arising from W decays, one can gain information about the u- and d-quark pdf ratios. The asymmetry is defined as

$$A(\eta) = \frac{N^+(\eta) - N^-(\eta)}{N^+(\eta) + N^-(\eta)},$$

where $N^+(\eta)$ is the number of events with a positive lepton in a positive region, or a negative lepton in a negative region (positive correlation), and $N^-(\eta)$ is defined conversely (negative correlation). Figure 13 shows the measured lepton charge

asymmetry versus the charged lepton's rapidity for CDF (electrons and muons)¹¹ and DØ (muons only). The most recent pdf fits now include the published CDF data.

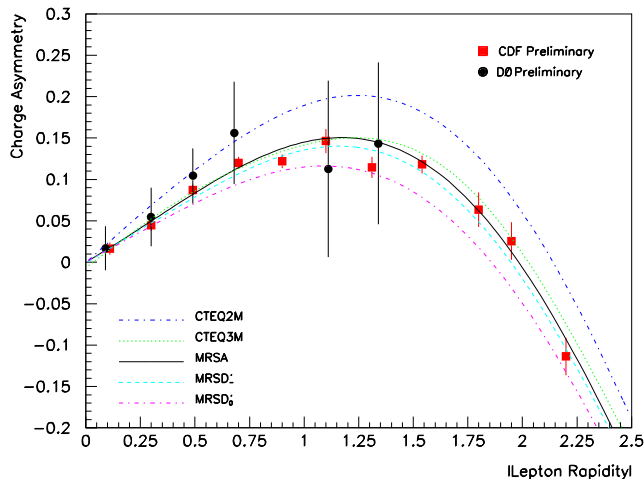


Fig. 13. The lepton charge asymmetry versus rapidity for W events.

5.1.3 Drell-Yan Production and Compositeness

CDF has complemented their previously published¹² Drell-Yan differential cross section with a preliminary analysis of their Run 1 data. The vastly improved statistics ($\simeq 110 \text{ pb}^{-1}$ versus $\simeq 4 \text{ pb}^{-1}$) have greatly extended the reach of this measurement as is shown in Fig. 14, which presents the differential cross section $d^2\sigma/dMdy$ for ee and $\mu\mu$ events detected in the central rapidity interval $|\eta| < 1$. The new data agree well with the previous measurement as well as being in very good agreement with NLO QCD predictions. The existence of an additional contact term interaction between quarks and leptons would affect the shape of the dilepton invariant mass distribution, enhancing the cross section at high dilepton invariant masses. As there is no appreciable excess, and assuming a contact interaction of the form proposed in Ref. 7, CDF has placed preliminary limits on this compositeness scale $\Lambda^{-(+)} > 2.5(3.8) \text{ TeV}$, where $\Lambda^{-(+)}$ correspond to constructive or destructive interference terms, respectively. These compositeness scale limits probe distances on the order of 10^{-17} cm .

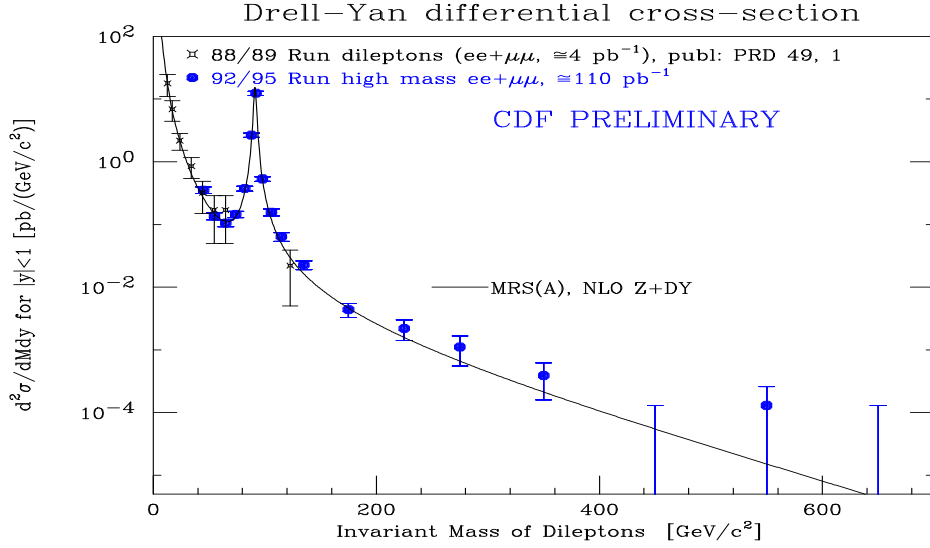


Fig. 14. The Drell-Yan ($ee + \mu\mu$) differential cross section $d^2\sigma/dMdy$ as measured by CDF.

5.2 Trilinear Gauge Boson Couplings

Trilinear gauge boson couplings are couplings between the W and Z bosons and photons, and are a direct consequence of the non-Abelian $SU(2) \times U(1)$ gauge symmetry of the electroweak interactions. Due to the very sensitive nature of the gauge cancellations, anomalous couplings, representing perhaps the substructure of the W and Z , will manifest themselves as enhancements in the cross section for associated boson production ($\bar{p}p \rightarrow WW, WZ, W\gamma, Z\gamma$), as well as modifications to the differential distributions. Probing these couplings provides therefore a crucial test of the gauge structure of the electroweak interaction.

As seen previously, precision cross-section measurements at the Tevatron are plagued by both experimental and theoretical uncertainties. A more sensitive test of the $WW\gamma$ vertex involves a fit to the photon E_T spectrum, since anomalous couplings would give rise to significantly more high E_T photons than the SM. The CP-conserving coupling parameters in the Lagrangian describing the $WW\gamma$ interaction, κ and λ , are related to the magnetic dipole moment (μ_W) and the electric quadrupole moment (Q_W) via the following relations:

$$\mu_W = \frac{e}{2m_W}(1 + \kappa + \lambda); \quad Q_W = \frac{-e}{m_W^2}(\kappa - \lambda).$$

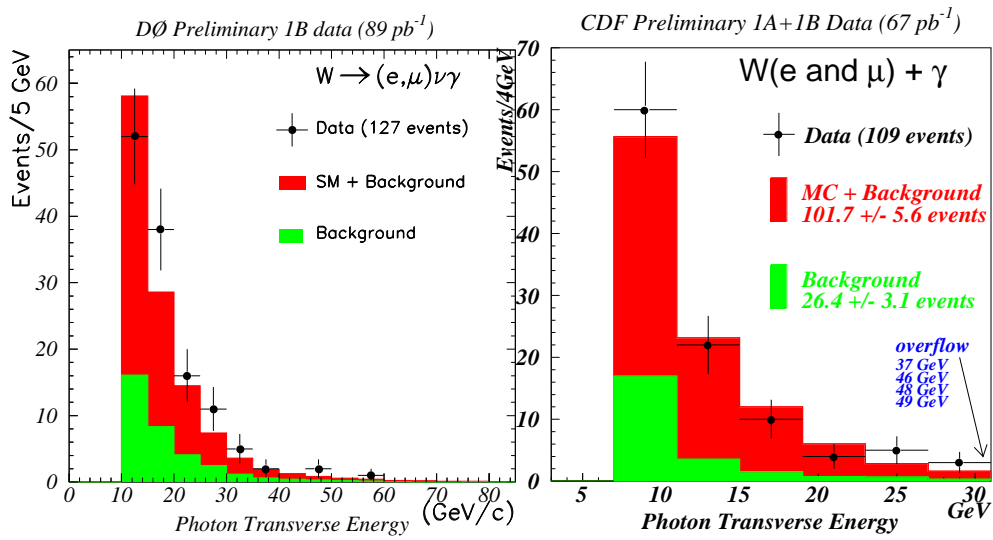


Fig. 15. The photon transverse energy distribution in $W\gamma$ candidate events for DØ (left) and CDF (right).

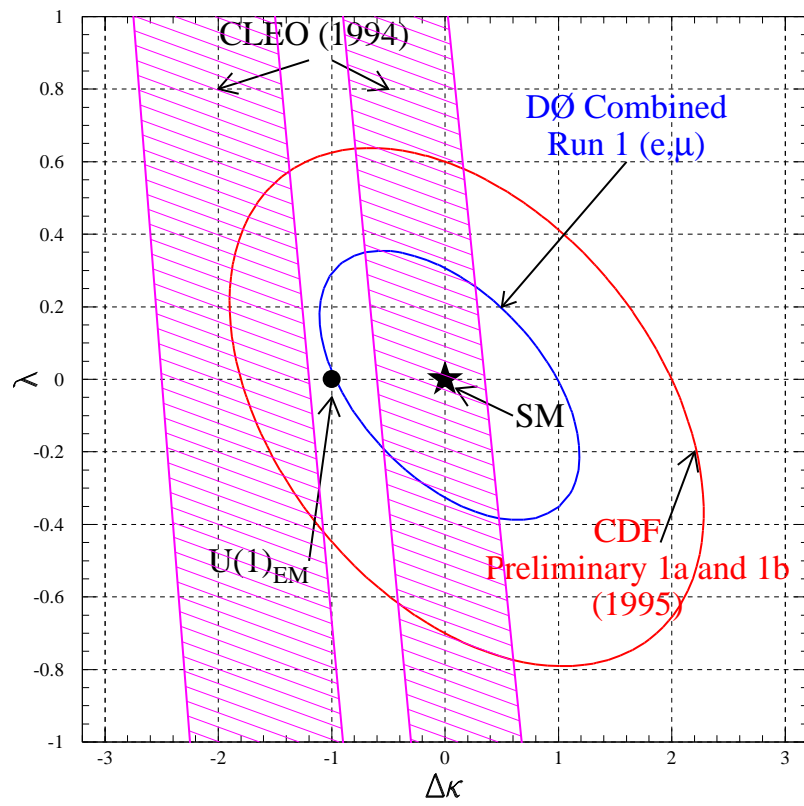


Fig. 16. Experimental limits on the $W - \gamma$ anomalous couplings λ and $\Delta\kappa$.

In the SM $\Delta\kappa(= \kappa - 1) = \lambda = 0$. Both CDF and DØ have completed preliminary analyses of their Run 1 data wherein events containing a high E_T e or μ and significant \cancel{E}_T (from the leptonic decay of the W boson) and a photon isolated from the lepton were selected. The photon E_T distribution was then fit to spectra generated from expected backgrounds plus Monte Carlo simulations of $W\gamma$ production with various values of the anomalous couplings. The photon E_T distributions as measured by the DØ and CDF experiments are shown in Fig. 15. Data are represented as points, with MC and background contributions shown as the shaded histograms, showing very good agreement between the measured and predicted spectra. Fits to MC photon E_T spectra generated with various values for the anomalous couplings are used to derive limits. In Fig. 16 are the 95% confidence level exclusion contours from the two collider experiments, as well as the results from the CLEO experiment.¹³ The complementarity of the two measurements is clearly seen. The DØ Collaboration has placed the following axis limits on these two couplings: $-0.97 < \Delta\kappa < 0.99(\lambda = 0)$ and $-0.33 < \lambda < 0.31(\Delta\kappa = 0)$. Note that for the first time, the strictly $U(1)_{EM}$ nature of the $W - \gamma$ interaction is being ruled out by experiment; the vector boson and photon interact through more than simply the charge of the W. Analyses of the remaining channels have also been conducted¹⁴ (the sensitivity is similar to the $W\gamma$ channels), with the results all being consistent with SM expectations.

5.3 The W Mass

Precision measurements of the W mass provide strong constraints on the SM. Within the SM the mass of the W vector boson at the Born level can be exactly predicted in terms of other fundamental parameters. However, the W mass is sensitive to higher order radiative corrections involving the top quark and Higgs masses. Therefore, a precision measurement of the W mass, combined with the top quark mass, provides insight into not only the current understanding of the SM by providing constraints in the Higgs sector, but also may, if inconsistent with the SM predictions, provide evidence for the existence of new phenomena above the electroweak scale.

The W mass analyses from CDF and DØ discussed here are based on the Run 1b data of 90 and 82 pb^{-1} , respectively. As mentioned previously, W bosons are detected by their decays into leptons and their associated neutrinos. The

recent CDF analysis of W decays into muons, and the DØ analysis of the electron final state are presented. Both experiments apply stringent selection criteria: central ($|\eta| \leq 1$), isolated, high p_T ($25 < p_T(\mu) < 60$ GeV, $p_T(e) > 25$ GeV) leptons, and large missing transverse energy (> 25 GeV) are required, resulting in data samples of 21,000 and 28,000 W bosons for the CDF and DØ analyses, respectively. Since the neutrino's longitudinal momentum is not measurable, the W boson mass must be extracted from transverse quantities. In this presentation, only mass determinations extracted from the transverse mass will be presented, although one could utilize the electron or muon transverse momentum, or the missing transverse energy in the event to determine the mass. Unlike the invariant mass, no analytic form for the transverse mass is available, so strong reliance is made on Monte Carlo simulation of the detectors to various hypothetical input W masses. It is essential that the detector response to both the W boson decay products and the recoiling hadronic system, including efficiencies and resolutions, be well-understood; the energy scale determines the leading edge of the transverse mass Jacobian distribution, and the resolutions determine the sharpness.

The absolute momentum scale of the CDF central tracking chamber is calibrated using a large ($\sim 250,000$) sample of $\psi \rightarrow \mu^+\mu^-$ events. Normalizing to the world average ψ mass yields a correction factor of 1.00023 ± 0.00048 . Extrapolating the uncertainty to M_W results in an uncertainty of 40 MeV due to the momentum scale. The p_T dependence of the momentum scale was studied both by considering the ψ mass as a function of P_T and also by studying the masses of the Υ and Z resonances. Figure 17 shows the difference between the measured $\Upsilon(1S)$ mass and the world average, along with the CDF simulation which includes energy loss, magnetic field variations, and geometrical misalignments. Figure 18 shows the ratio of measured to world average mass (i.e., the momentum scale factor) for the various resonances. The observed dependence on mass is not corrected, but is included in the systematic uncertainty; the shaded region defines the uncertainty caused by extrapolating to the momentum scale of the W decay muons.

The electron energy scale at DØ is determined primarily by calibrating to the Z resonance via its decay to electron pairs. Test beam measurements of the energy response of the DØ electromagnetic calorimeter provide strong evidence for a linear relationship between observed and true energy. The scale (α) and offset (δ) of the calorimeter response is set by analyzing Z boson and J/ψ decays to electrons, as well as reconstructing π^0 decays in the central calorimeter.

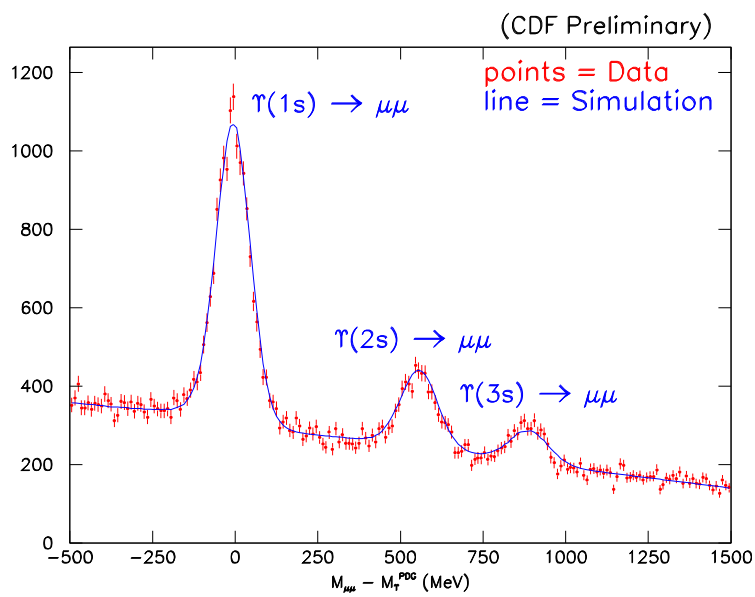


Fig. 17. The CDF momentum scale at the Υ . Shown is the mass difference between the reconstructed $\Upsilon(1S)$ mass and the world average M_{Υ} . Data are represented by points; the solid curve is the best fit to a simulated lineshape which includes the detector response.

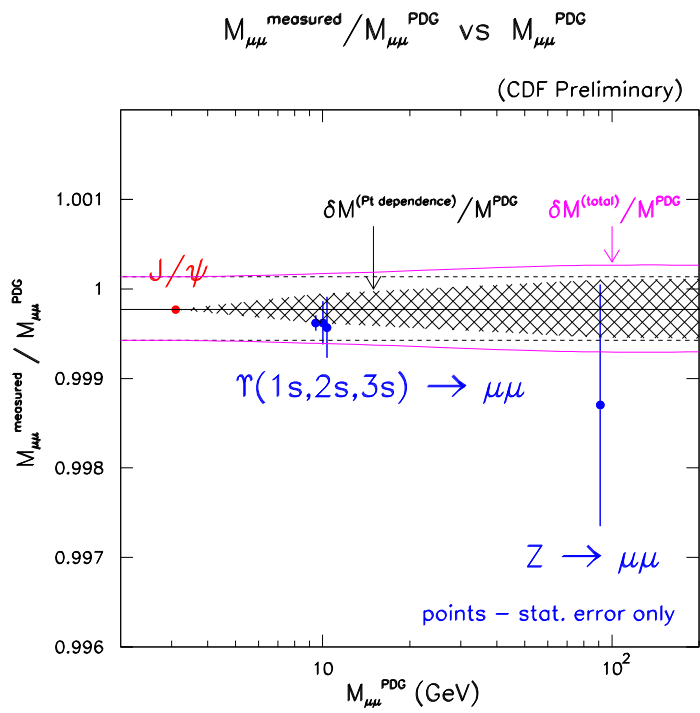


Fig. 18. The CDF momentum scale uncertainty propagated from the ψ resonance to the Z.

Figure 19 shows the reconstructed $\psi \rightarrow e^+e^-$ invariant mass as well as the $\pi^0 \rightarrow \gamma\gamma$ symmetric mass. The π^0 reconstruction is based on events where both photons convert in the inner tracker volume, giving rise to two tracks whose dE/dx is consistent with two particles. The resulting EM showers are not resolved in the calorimeter, but from the shower energy and the track opening angle, one can construct a symmetric mass (so named since one assumes the π^0 energy to have been evenly shared between the photons). Each of the three resonances has a different sensitivity to the scale and offset of the calorimeter response. The combined fit (shown in Fig. 20) yields $\alpha = 0.9533 \pm 0.0008$ and $\delta = -0.160^{+0.03}_{-0.21}$. This results in an uncertainty on the W boson mass due to the energy scale of 70 MeV, dominated by the limited Z statistics.

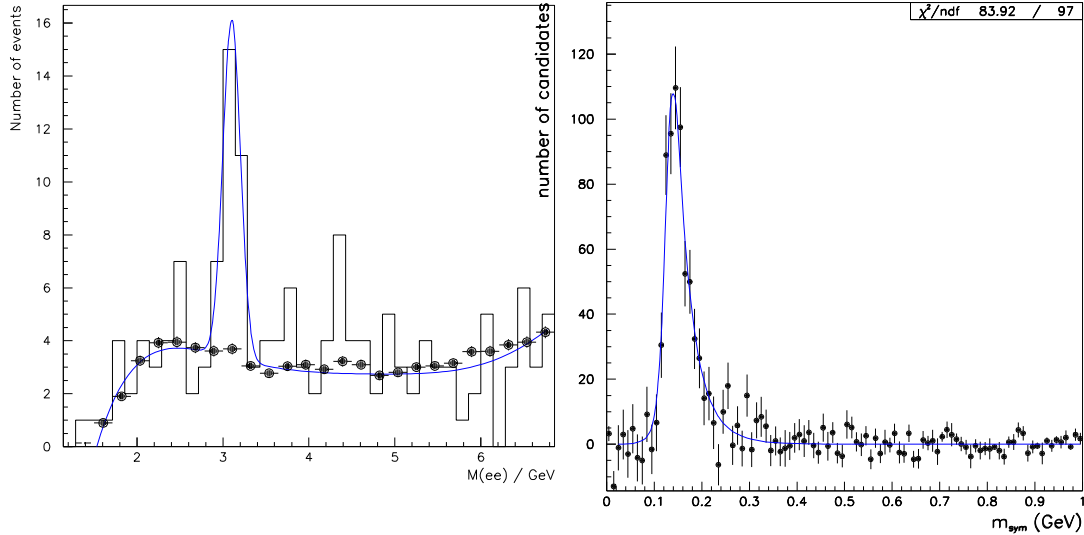


Fig. 19. The $\psi \rightarrow e^+e^-$ invariant mass, and the $\pi^0 \rightarrow \gamma\gamma$ symmetric mass (see text), used to determine the $D\bar{O}$ energy scale.

The calorimeter response to the recoiling system is determined by comparing the p_T of the recoil system to the p_T of the dileptons in Z events. The effects of the underlying event are derived from an analysis of minimum bias data.

With the detector response well-understood, transverse mass line shapes are generated by simulating the response to millions of Monte Carlo events generated at various values of the W boson mass. The transverse momentum and rapidity of the boson are sampled from the parameterization due to Ladinsky and Yuan.¹⁵

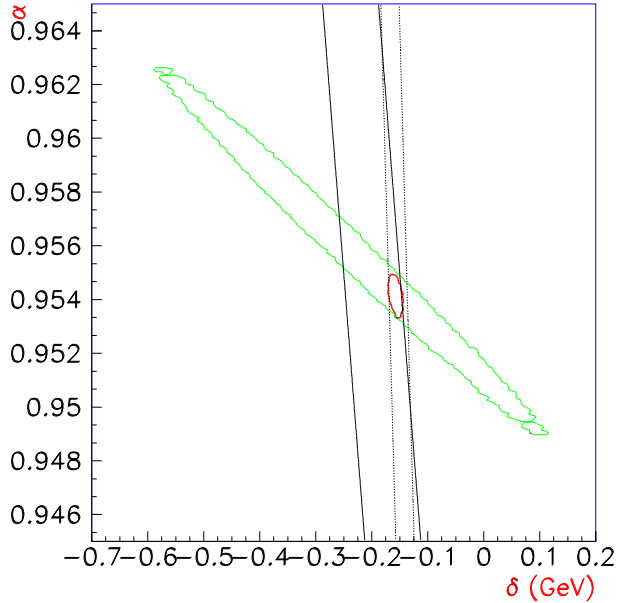


Fig. 20. Limits on the energy scale (α) and offset (δ) of the DØ calorimeter, derived from π^0 , ψ , and Z resonance data.

The mass is selected from a relativistic Breit-Wigner distribution convoluted with parton luminosity distributions. The bosons are forced to decay, correctly accounting for the polarization and including radiative decays. The effects of W decays to τ , with subsequent leptonic decay of the τ , are also simulated. The lepton energy and direction are smeared according to the detector response, as is the W recoil. The underlying event is modeled by including minimum-trigger-bias events at the appropriate luminosity. Detector and trigger acceptance and efficiencies are also included at this stage. The transverse mass distribution is then generated for various input W masses.

Unbinned maximum likelihood fits are performed to the data and Monte Carlo template spectra, providing the best-fit W mass. DØ repeats the process for the Z boson effective mass to extract the W/Z mass ratio. Figure 21 presents the transverse mass distribution for the data, along with the results of the fit for the CDF $W \rightarrow \mu\nu$ analysis. The fit was conducted in the region $65 < m_T < 100$ GeV resulting in a best-fit $M_W^\mu = 80.430 \pm 0.100(stat.)$ GeV. The corresponding plot for the DØ $W \rightarrow e\nu$ analysis is shown in Fig. 22. The fit (performed in the region $60 < m_T < 90$ GeV) provides $M_W^e = 80.450 \pm 0.070(stat.)$ GeV.

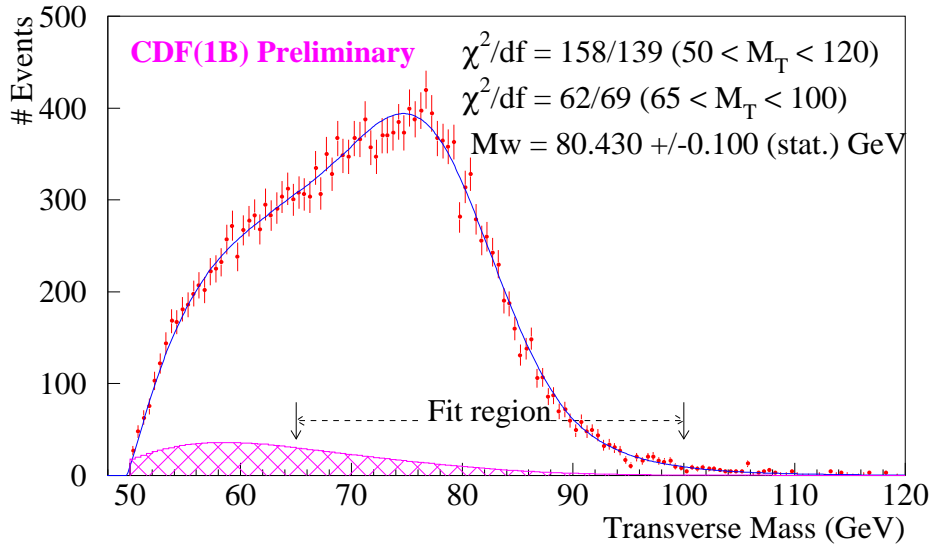


Fig. 21. The transverse mass distribution for W boson decays into muons as measured by CDF from the Run 1 data sample, as well as results of the fits.

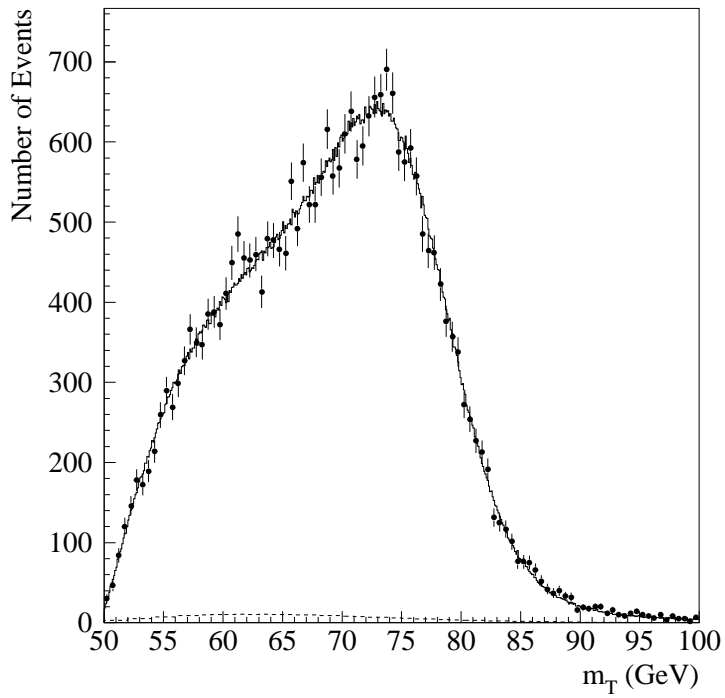


Fig. 22. The transverse mass distribution for W boson decays into electrons as measured by DØ from the Run 1 data sample.

A full accounting of the systematic uncertainties in these measurements lies outside the scope of this article. A summary of the uncertainties in the W mass measurement is presented in Table 2. Full details are available in the references.^{16,17,18} The final W boson masses from these two analyses are then:

$$M_W^\mu = 80.430 \pm 0.100(\text{stat.}) \pm 0.120(\text{syst.}) \text{ GeV},$$

$$M_W^e = 80.450 \pm 0.070(\text{stat.}) \pm 0.95(\text{syst.}) \text{ GeV}.$$

The measured values are seen to be in very good agreement with one another. Combining these values with previous measurements,^{16,17} those of the UA2 experiment,¹⁹ the values from LEP,²⁰ and taking into account correlations in the uncertainties, yields a value for the W boson mass of:

$$M_W \text{ (world preliminary)} = 80.400 \pm 0.075 \text{ GeV}.$$

These results are presented graphically in Fig. 23.

As mentioned earlier, within the SM, the masses of the W boson, the top quark, and the Higgs boson are interconnected. Figure 24 presents this relationship for various putative Higgs masses. The W boson and top quark masses as measured at the Tevatron are plotted, as are the constraints implied by the electroweak measurements from LEP and SLD. The data are in good agreement with the SM predictions, although the uncertainties are still too large to make any strong statements about the Higgs mass. Data from Run 1 continue to be analyzed by both collaborations; CDF intends to finalize its mass analysis in the electron channel, and DØ will soon complete its analysis of electrons in the forward regions. The uncertainty in the W mass from the collider experiments is then expected to approach ~ 70 MeV.

6 Conclusions

The high energy of the Tevatron and large data samples collected during the last run have allowed many precision measurements to be undertaken. Recent results of selected topics in the fields of QCD jet physics and electroweak interactions have been presented.

Analyses of the inclusive jet production cross section have demonstrated a remarkable agreement between the prediction of NLO QCD and experimental

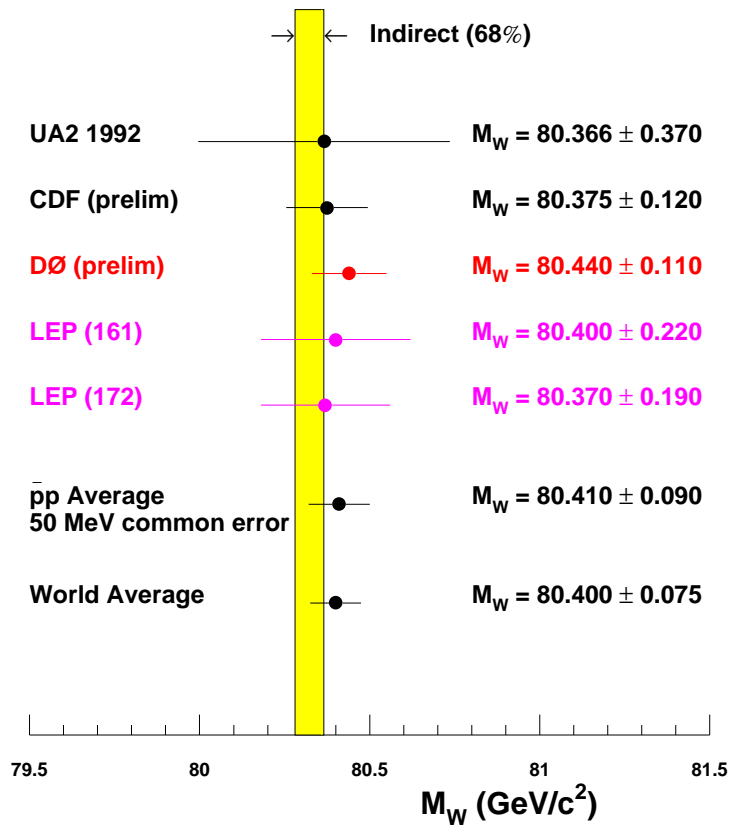


Fig. 23. Graphical representation of experimental values of the W boson mass, along with the current world average.

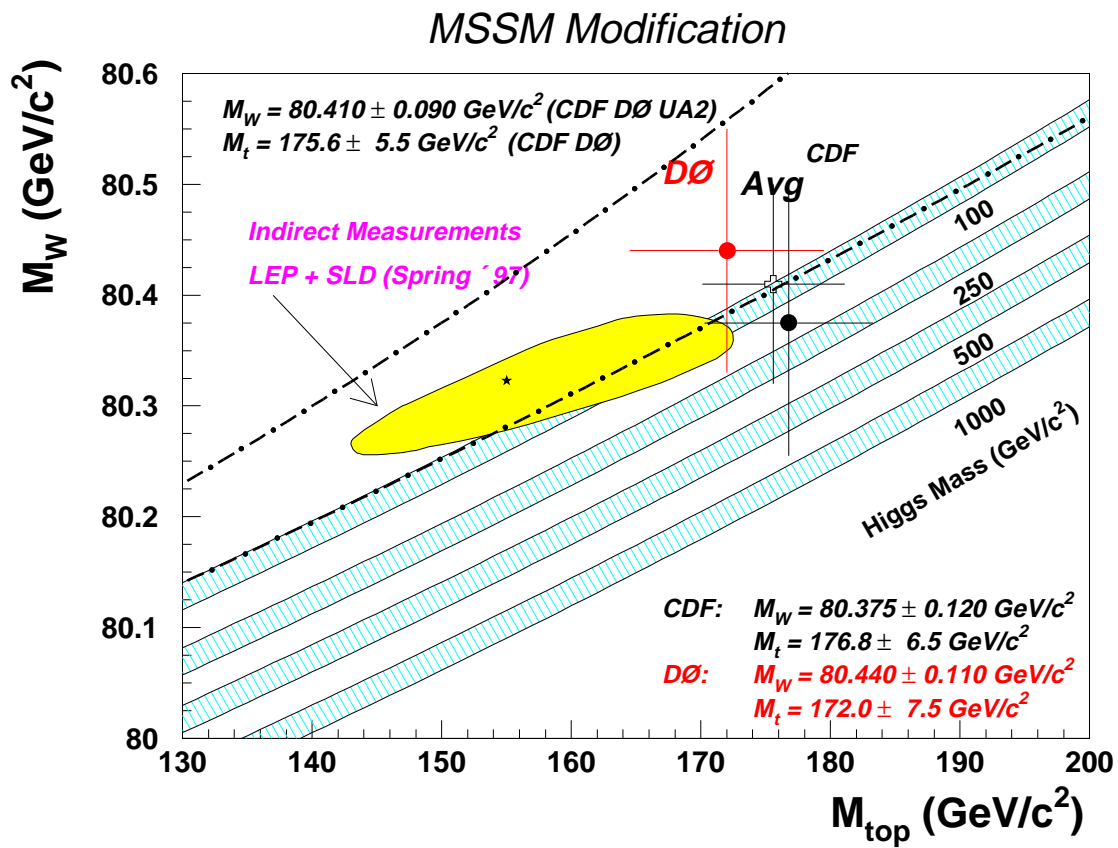


Fig. 24. Standard Model predictions for the relationship between the W boson mass and the top quark mass, for various Higgs boson masses.

measurements, spanning seven orders of magnitude. Although there may exist some discrepancy in interpretation at the highest transverse energies, there is at present no need to invoke new physics processes to explain the data. The data sets from the two experiments agree within uncertainties; the major difference in interpretation arises from different choices for theoretical models. The measurement of the dijet angular distribution affords a more sensitive test of NLO predictions. Quark compositeness, modeled via a contact interaction, can be ruled out at mass scales $\Lambda \leq 2$ TeV. Next-to-leading-order quantum chromodynamics does a very good job of explaining jet production at the Tevatron.

In the electroweak sector, W and Z boson production rates and decay characteristics are in accord with SM predictions. Analyses of the width of the W resonance limit non-SM decays of the W to $\Gamma < 109$ MeV. Quark-gluon compositeness limits have been extended to mass scales of $\Lambda = 2.5\text{--}6$ TeV through an analysis of Drell-Yan dilepton production. The trilinear gauge boson coupling between the W boson and the photon demonstrates that the W is truly a gauge boson, interacting with the photon through more than just its charge. Anomalous couplings, which would have indicated a possible substructure of the W boson, have been ruled out at ever stricter levels. Finally, the mass of the W boson has been measured more precisely than ever before. Although not yet precise enough to constrain the mass of the Higgs boson (in conjunction with the top quark mass, also measured at the Tevatron), the value of $M_W^{pp} = 80.410 \pm 0.090$ GeV is fully consistent with SM expectations. There are, as yet, no experimental disagreements with the SM.

Both collider experiments, as well as the accelerator, are undergoing aggressive upgrades. The advent of the Main Injector upgrade to the Tevatron promises a substantial increase in the luminosity to be delivered to each experiment. Detector upgrades will allow more and better information to be gathered from each interaction; CDF is improving on many aspects of its detector, while DØ is adding a central magnetic field with a new scintillating fiber central tracker and silicon microvertex detector. Both experiments are preparing to accumulate ~ 2 fb⁻¹ of integrated luminosity during the next run, which is expected to commence at the turn of the millennium.

Many of the results which have been presented are preliminary in nature, while others represent the final analyses and have been, or will shortly be, published. A few of the results have already been superceded, due to the passage of time

between the presentation of this talk and the publication of these proceedings. It should also be stressed that many more analyses are underway, mining the large and very rich data sample. Both collider detectors maintain sites on the World Wide Web,²¹ where up-to-date summaries and descriptions of these and other analyses can be found. The interested reader is directed to them for current and additional information.

Acknowledgments

I would like to thank the organizers of the Summer Institute for providing a stimulating environment in which to present this talk. Both collaborations extend thanks to their respective funding agencies.

References

- [1] S. Abachi *et al.*, Nucl. Instrum. Methods A **338**, 185 (1994); F. Abe *et al.*, Nucl. Instrum. Methods A **271**, 376 (1988).
- [2] S. D. Ellis, Z. Kunszt, and D. Soper, Phys. Rev. D **64**, 2121 (1990).
- [3] W. Giele, E. W. N. Glover, and D. A. Kosower, FERMILAB-PUB-94/070-T (1994).
- [4] F. Abe *et al.*, Phys. Rev. Lett. **77**, 438 (1996).
- [5] F. Abe *et al.*, Phys. Rev. Lett. **77**, 5336 (1996); Erratum *ibid.* **78**, 4307 (1997).
- [6] B. Abbott *et al.*, Phys. Rev. Lett. **80**, 666 (1998).
- [7] E. Eichten, K. Lane, and M. Peskin, Phys. Rev. Lett. **50**, 811 (1983).
- [8] S. Abachi *et al.*, Phys. Rev. Lett. **75**, 1456 (1995).
- [9] F. Abe *et al.*, Phys. Rev. Lett. **76**, 3070 (1996).
- [10] F. Abe *et al.*, Phys. Rev. Lett. **74**, 341 (1995).
- [11] F. Abe *et al.*, Phys. Rev. Lett. **74**, 850 (1995).
- [12] F. Abe *et al.*, Phys. Rev. D **49**, 1 (1994).
- [13] S. Playfer *et al.*, Int. J. Mod. Phys. A **10**, 4107 (1995).
- [14] F. Abe *et al.*, Phys. Rev. Lett. **74**, 1936, (1995); *ibid.* **74**, 1941 (1995); S. Abachi *et al.*, Phys. Rev. Lett. **75**, 1028, (1995); *ibid.* **75**, 1034 (1995); S. Abachi *et al.*, Phys. Rev. Lett. **78**, 3634 (1997); *ibid.* **78**, 3640 (1997); S. Abachi *et al.*, Phys. Rev. D **56**, 6742 (1997);

- B. Abbott *et al.*, Phys. Rev. Lett. **79**, 1441 (1997);
B. Abbott *et al.*, Phys. Rev. D (accepted), Fermilab-Pub-97/363-E;
B. Abbott *et al.*, submitted to Phys. Rev. D, Rapid Communications,
Fermilab-Pub-98/076-E;
B. Abbott *et al.*, submitted to Phys. Rev. D, Rapid Communications,
Fermilab-Pub-98/094-E.
- [15] G. Ladinsky and C.-P. Yuan Phys. Rev. D **50**, 4239 (1994).
- [16] F. Abe *et al.*, Phys. Rev. Lett. **65**, 2243 (1990);
F. Abe *et al.*, Phys. Rev. D **43**, 2070 (1991);
F. Abe *et al.*, Phys. Rev. Lett. **75**, 11 (1995);
F. Abe *et al.*, Phys. Rev. D **52**, 4784 (1995).
- [17] S. Abachi *et al.*, Phys. Rev. Lett. **77**, 3309 (1996);
B. Abbott *et al.*, Phys. Rev. D. (to be published), Fermilab-Pub-97/328-E.
- [18] B. Abbott *et al.*, Phys. Rev. Lett. **80**, 3008 (1998);
B. Abbott *et al.*, Phys. Rev. D (submitted), Fermilab-Pub-97/422-E.
- [19] J. Alitti *et al.*, Phys. Lett. B **276**, 354 (1992).
- [20] The LEP Experiments, CERN-PPE 97/154;
ALEPH: CERN-PPE 97/164;
DELPHI: Eur. Phys. J. C **1**, 395 (1998);
L3: Phys. Lett. B **413**, 176 (1997);
OPAL: CERN-PPE 97/116.
- [21] "<http://www-cdf.fnal.gov/>",
 "<http://www-d0.fnal.gov/>".

Source	CDF	DØ
	μ	e
Statistical	100	70
Energy/Momentum Scale	40	65
Calorimeter Linearity	-	20
Lepton Angle	-	30
e or μ Resolution	25	25
Recoil Model	90	40
p_T^W Model, pdf's	50	25
Radiative Decays	20	20
QCD/QED Cor's	20	-
W-Width	-	10
Backgrounds/Bias	30	10
Fitting Procedure	10	-
Systematic	115	70
Total Uncertainty	155	120

Table 2. Uncertainties in the W mass measurements in MeV.